Pectin Chemistry and Cellulose Crystallinity Govern Pavement Cell Morphogenesis in a Multi-Step Mechanism[1][OPEN]

Bara Altartouri,[a] Amir J Bidhendi,[a] Tomomi Tani,[b] Johnny Suzuki,[c] Christina Conrad,[c] Youssef Chebli,[d] Na Liu,[e] Chithra Karunakaran,[e] Giuliano Scarcelli,[c] and Anja Geitmann[a,d,2,3]

[a]Département de Sciences Biologiques, Université de Montréal, Montréal, QC H1X2B2, Canada
[b]Eugene Bell Center for Regenerative Biology and Tissue Engineering, Marine Biological Laboratory, Woods Hole, Massachusetts 02542
[c]Fischell Department of Engineering, University of Maryland, College Park, Maryland 20742
[d]Department of Plant Science, McGill University, Sainte-Anne-de-Bellevue, QC H9X3V9, Canada
[e]Canadian Light Source, Saskatoon, SK S7N2V3, Canada

ORCID IDs: 0000-0002-9148-640X (B.A.); 0000-0002-7482-7444 (A.J.B.); 0000-0003-4472-7714 (T.T.); 0000-0001-8688-2523 (C.C.); 0000-0003-0390-0517 (A.G.).

Simple plant cell morphologies, such as cylindrical shoot cells, are determined by the extensibility pattern of the primary cell wall, which is thought to be largely dominated by cellulose microfibrils, but the mechanism leading to more complex shapes, such as the interdigitated patterns in the epidermis of many eudicotyledon leaves, is much less well understood. Details about the manner in which cell wall polymers at the periclinal wall regulate the morphogenetic process in epidermal pavement cells and mechanistic information about the initial steps leading to the characteristic undulations in the cell borders are elusive. Here, we used genetics and recently developed cell mechanical and imaging methods to study the impact of the spatio-temporal dynamics of cellulose and homogalacturonan pectin distribution during lobe formation in the epidermal pavement cells of Arabidopsis (*Arabidopsis thaliana*) cotyledons. We show that nonuniform distribution of cellulose microfibrils and demethylated pectin coincides with spatial differences in cell wall stiffness but may intervene at different developmental stages. We also show that lobe period can be reduced when demethyl-esterification of pectins increases under conditions of reduced cellulose crystallinity. Our data suggest that lobe initiation involves a modulation of cell wall stiffness through local enrichment in demethylated pectin, whereas subsequent increase in lobe amplitude is mediated by the stress-induced deposition of aligned cellulose microfibrils. Our results reveal a key role of noncellulosic polymers in the biomechanical regulation of cell morphogenesis.

Cellular differentiation in plants involves dramatic alterations in cell shape leading to highly specialized cell types, such as trichomes, fibers, or guard cells. Cell growth and shaping involve a turgor-driven deformation of the cell wall and are assumed to be governed by at least two crucial parameters related to the material properties of the primary cell wall (Altartouri and Geitmann, 2015; Sanati Nezhad and Geitmann, 2015). The first parameter is the degree of spatial uniformity of the wall stiffness that is controlled by the extensibility of the cell wall material and the dimensions (thickness) of the wall. The second parameter is the degree of anisotropy of the wall material properties that control the directionality of the expansion. These parameters can be modulated by the local addition of stiffer or softer cell wall material (Zerzour et al., 2009; Chebli et al., 2012; Szymanski, 2014; Peaucelle et al., 2015; Yanagisawa et al., 2018) and/or by the local secretion of enzymes or wall modulating agents that break existing linkages between polymers (Cosgrove, 1998, 2016). Cellular processes such as exocytosis, polymer synthesis, and wall assembly thus determine the expansion pattern of individual plant cells and consequently the morphogenesis of complex tissues (Szymanski and Cosgrove, 2009; Szymanski and Staiger, 2018). Cellulose microfibrils play a major role in determining the

expansion directionality of the plant cell wall. When these polymers are arranged in nonrandom manner in the plane of the cell wall, they restrict expansion in parallel but allow expansion in the direction perpendicular to their net orientation (Diddens et al., 2008; Anderson et al., 2010). This is related to the strong tensile strength these polymers exhibit along their long axis, which increases with increased degree of structural order of the microfibrils (i.e. crystallinity; Eichhorn and Young, 2001; Kerstens et al., 2001; Thomas et al., 2013; Cosgrove, 2014). Mutation or drug-induced reduction in cellulose crystallinity causes radial swelling of cylindrical cells (Aouar et al., 2010; Fujita et al., 2013). While the concepts of cell shaping are increasingly well characterized in geometrically simple shapes, such as the cylindrical cells of the shoot and root, the mechanism of complex shape formation remains poorly understood.

The epidermal layer of eudicotyledon leaves exhibits several types of such complex cell geometries that are generated from a simple shape: trichomes, guard cells, and pavement cells. Depending on the species, pavement cells can be brick-shaped or they form an inter-digitated jigsaw-puzzle pattern, with indents (necks) and protrusions (lobes) of neighboring cells being tightly connected to each other and forming undulations. This phenomenon is widely distributed, although with substantial variations (Vőfély et al., 2019). The lobed pattern has been proposed to reduce the stress in the periclinal walls of larger epidermal cells (Sapala et al., 2018). Our understanding of the shape formation and developmental processes at the cellular level is largely based on inferences made from the observations of cytoskeletal dynamics (Fu et al., 2005; Panteris and Galatis, 2005; Kotzer and Wasteneys, 2006; Zhang et al., 2011; Szymanski, 2014; Armour et al., 2015; Eng and Sampathkumar, 2018). Because cytoskeletal proteins are easier to observe in living cells than cell wall polysaccharides, and because the deposition of the latter is often regulated by the former, cytoskeletal dynamics are frequently used as a proxy for developmental changes occurring in the cell wall. Notably, it has been hypothesized that the spatial arrangement of cortical microtubules alters cell wall stiffness through deposition of cellulose microfibrils to restrict the expansion of the cell at neck regions of pavement cells, while lobe regions continue to expand during cell growth (Panteris and Galatis, 2005; Szymanski, 2014; Armour et al., 2015). Although there is evidence for the correspondence between the alignment of cortical microtubules with the expansion direction in which cellulose microfibrils are deposited, for instance, in the cylindrical epidermal cells of plant roots (Anderson et al., 2010), there is no clear evidence for such correspondence in the lobe formation of pavement cells. Cellulose microfibrils are arranged in a fan-like configuration in the neck regions of the periclinal wall in pavement cells of several eudicotyledons (Panteris et al., 1994; Panteris and Galatis, 2005), but so far this has only been shown for mature cells of Arabidopsis (*Arabidopsis thaliana*) that possess fully developed lobes (Sampathkumar et al., 2014), whereas information on early developmental stages is elusive. This arrangement of cellulose microfibrils at the neck region is thought to allow the wall to expand perpendicularly to the direction of the microfibrils and, thus, initiate waviness (Panteris and Galatis, 2005; Szymanski, 2014). At the lobe region of the periclinal wall, two configurations of cellulose microfibrils are suggested: A net-like configuration that allows isotropic expansion of the lobe region (Armour et al., 2015), and an arrangement parallel to the tangent of the lobe tip that allows anisotropic expansion toward the long axis of the lobe (Szymanski, 2014; Elsner et al., 2018). A recent study showed that treatment with cellulase alters Arabidopsis pavement cell shape, but does not prevent the generation of waviness (Higaki et al., 2017). The exact role of cellulose microfibrils at various stages of pavement cell development has not been examined. In silico simulation predicts an important role for the stress-induced deposition of cellulose microfibrils during the development of wavy cell shapes (Sampathkumar et al., 2014; Armour et al., 2015; Bidhendi et al., 2019; Bidhendi and Geitmann, 2019a). However, whether cellulose actually contributes to or is essential for the early stages of lobe formation is unknown.

The differentiation of pavement cells is proposed to be governed by spatial variations in the expansion rate of the periclinal wall between the opposing sides of the undulation (Armour et al., 2015; Bidhendi et al., 2019). Such spatial variation suggests the presence of subcellular variation in cell wall stiffness. This is supported conceptually by recent studies on shoot epidermal cells and pollen tubes (Zerzour et al., 2009; Chebli et al., 2012; Peaucelle et al., 2015). It has been shown that differences in the stiffness of the anticlinal walls of the shoot epidermal cells are required to promote cell elongation. The spatial difference in cell wall stiffness in these cells was regulated by the activity of pectin methyl esterase (PME), an enzyme that promotes gelation of the homogalacturonan (HG) pectin because it removes methyl-groups rendering the polymers negatively charged (Peaucelle et al., 2015; Bou Daher et al., 2018). Similarly, in the rapidly growing pollen tube, the local stiffness of the cell wall varies with softer material characterizing the growing region of the cell (Zerzour et al., 2009). This subcellular variation in cell wall stiffness reflects the spatial distribution of cell wall polymers (Fayant et al., 2010; Chebli et al., 2012). For pavement cells, various scenarios have been proposed to explain the formation of undulations, including a cellulose-based stiffening in the periclinal wall (Panteris and Galatis, 2005; Bidhendi et al., 2019; Bidhendi and Geitmann, 2019a) or the presence of mechanochemical heterogeneities in the adjacent anticlinal walls (Majda et al., 2017, 2019). The latter scenario is based on the presence of softer wall components, such as galactans and arabinans, at the neck region of the anticlinal wall, but the role of cellulose microfibrils was not examined. The external periclinal wall of pavement cells is suggested

to have a major role during lobe formation (Panteris and Galatis, 2005; Sampathkumar et al., 2014; Bidhendi and Geitmann, 2019a). Panteris et al. (1994) show that in *Cyperus papyrus* pavement cells, cortical microtubules bundle at the periclinal wall and that these bundles are not extended into the depth of the anticlinal wall. The depth of the anticlinal wall does not exhibit waviness in this species, pointing at an important role for cellulose microfibrils for the propagation of the morphogenetic process in 3D space (Bidhendi et al., 2019). Here, we investigate the role of cellulose microfibrils and demethyl-esterified pectin during the morphogenetic process of lobe development, focusing on the initiation of the process at the periclinal wall. We used live cell imaging to study the arrangement of the cellulose microfibrils at high spatial resolution and the distribution of the demethyl-esterified pectin in the pavement cells of the cotyledon of the Arabidopsis wild type and *anisotropy1* (*any1*) mutant, which is characterized by a significant reduction in cellulose crystallinity without reduction in overall cellulose content (Fujita et al., 2013). Moreover, we used Brillouin microscopy to infer the spatial stiffness map of the periclinal wall in living pavement cells. Finally, we tested the influence of the PME and PME inhibitor (PMEI) on the shape of pavement cells. The results of this study provide crucial evidence for the initiation mechanism of cell shaping and the roles of cellulose microfibrils and demethyl-esterified pectin during the developmental process of the undulations of pavement cells.

RESULTS

Lobes Can Be Initiated at a Substantially Reduced Degree of Cellulose Crystallinity

To understand the role of crystalline cellulose during lobe development, we investigated pavement cell shape in cotyledons of wild-type Arabidopsis and of the *any1* mutant (Fig. 1A; Supplemental Fig. S1). The total content of cellulose in the cell wall of this mutant was reported to be unaltered, while the relative amount of crystalline cellulose is reduced substantially. Moreover, epidermal pavement cells in this mutant have a swelling phenotype (Fujita et al., 2013). As this is thought to be caused by the reduced degree of cellulose crystallinity and hence reduced stiffness of the cell wall, we wanted to quantitatively assess the effect of this modulation in the wall molecular configuration on the lobed shape of the pavement cells. To this end, we measured the circularity ratio and the number of lobes per cell. Circularity is used here to evaluate shape changes of pavement cells during their developmental stages (Fig. 1A) as was done in previous works (Zhang et al., 2011; Armour et al., 2015). The circularity ratio is a number between 1 and 0, with 1 indicating a perfect circle. In *any1* the mean cell circularity ratio was significantly higher compared to the wild-type pavement cells at 2, 3, and 4 d after germination ($P < 0.001$;

Fig. 1B). While the circularity ratio decreased over the course of 2 d in the wild type, the value remained almost unaltered in the mutant over the same period of time. The decrease in circularity ratio does not discriminate between a potential increase in depth of existing undulations and the increase in the number of undulations. To untangle the two, we quantified the number of lobes and determined the aspect ratio of individual lobes. Only true lobes were taken into account, and newly dividing cells were excluded as detailed in Supplemental Note S1, Supplemental Figure S2, and Figure 1G. We then applied a convex hull-fitting algorithm on the shape of pavement cell and calculated the period of lobes by dividing the square root of the convex hull area by the lobe number. This ratio was chosen to exclude any differences between wild type and *any1* that are generated from the difference in the overall growth of the cell (Fig. 1, C, D, and G; Supplemental Fig. S2B). The mean lobe period in the *any1* mutant was significantly different from the wild type over the 4-d observation period (Fig. 1E). The aspect ratio of lobes was determined by calculating the depth over the width of a given lobe (Fig. 1, F and G). This parameter showed that lobes in *any1* were shallow compared to the wild-type pavement cells when observed at 4 d after germination. Importantly, this difference was generated by cellular development over the preceding 3 d, because at 1 d after germination the lobe aspect ratio was identical in *any1* and the wild type (Fig. 1F). While the lobe period was increased compared to the wild type, *any1* cells initiated lobes during pavement cell differentiation. Clearly, the amplitude of these lobes is not further increased during subsequent developmental steps. This suggests that high crystallinity is more critical for lobe expansion than for lobe initiation.

Well-Aligned Cellulose Microfibrils Are Required for Lobe Expansion More than Lobe Initiation

In several plant species, the alignment of cellulose microfibrils at the neck regions of mature pavement cells is fan-like, radiating from the tip of the neck (Panteris et al., 1994; Panteris and Galatis, 2005). Such orientation was shown for the neck region of young and fully formed pavement cell undulations in Arabidopsis cotyledons (Sampathkumar et al., 2014; Bidhendi et al., 2019). It is suggested that the perpendicular alignment restricts the expansion of the neck region, but there is no direct evidence for this association in the early stages of lobe formation. To examine whether lobe initiation and subsequent expansion in the wild-type and *any1* pavement cells is associated with the reported alignment of the cellulose microfibrils, we investigated the degree of the alignment (the anisotropy degree, hereafter) of cellulose at both neck and lobe regions with high spatial resolution in living cells. We stained cellulose microfibrils with the fluorescent dye Pontamine Fast Scarlet 4B (S4B), which specifically binds to cellulose

(Anderson et al., 2010), and used polarized fluorescence microscopy (Mehta et al., 2016; Swaminathan et al., 2017) to examine the anisotropy degree of cellulose microfibrils (Thomas et al., 2017). The anisotropy of S4B's fluorescence polarization reflects the anisotropy degree of cellulose in the periclinal wall of the pavement cells at pixel-by-pixel resolution. The reliability of this technique for determining the molecular alignment of cellulose in plant cell walls was confirmed by testing it on plant cells whose cellulose microfibril orientation is well established (Supplemental Fig. S3, A and B). These calibration tests suggest that the ensemble fluorescence polarization orientation of S4B bound to

cellulose is parallel to the orientation of cellulose microfibrils.

At later developmental stages, cellulose microfibrils on the neck side of an undulation had a preferential orientation perpendicular or fan-like to the tangent at the tip of the undulation (Fig. 2A; Supplemental Fig. S3, C and D). This is in agreement with what was previously suggested (Sampathkumar et al., 2014) and the reported orientation of the microfibrils in developed pavement cells (Panteris et al., 1994; Panteris and Galatis, 2005; Bidhendi et al., 2019). More importantly, we were able to quantify the anisotropy degree of cellulose microfibrils at subcellular resolution in the
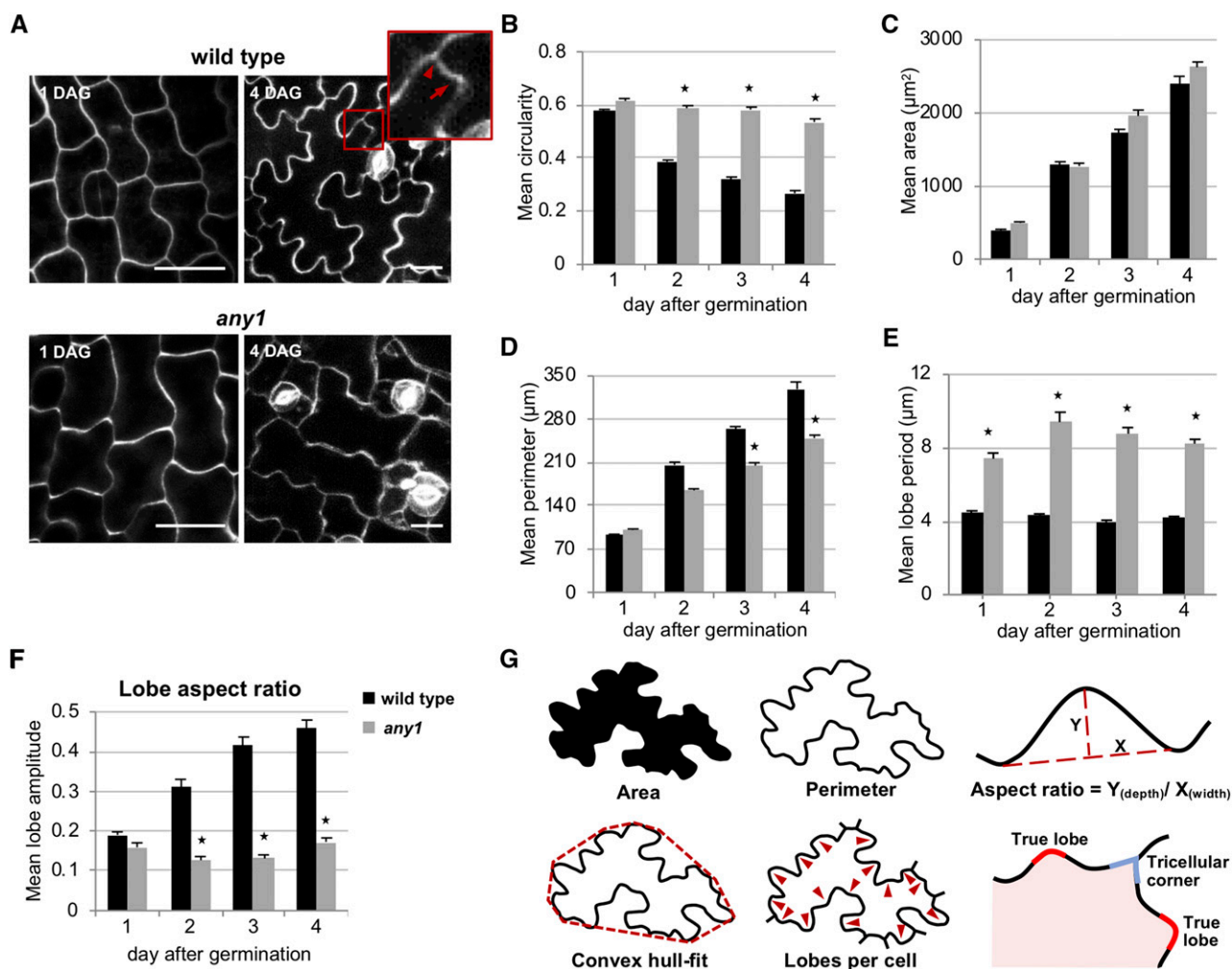
Figure 1. Shape analysis of Arabidopsis pavement cells of wild type and *any1*. A, Fluorescence micrographs of pavement cells on the abaxial side of a cotyledon at 1 d (left) and 4 d (right) after germination of wild type (upper row) and *any1* (lower row) stained with PI. Scale bars = 20 μm. Cell border enclosed in the red rectangle is magnified to show the difference between true lobe (arrow) and tricellular junction (arrowhead). B to F, Developmental changes in the mean circularity (B), cell area (C), cell perimeter (D), lobe period (E), and lobe aspect ratio (F) of the wild-type (black bars) and *any1* (gray bars) pavement cells from 1 to 4 d after germination. Lobe period equals square root of convex hull area divided by number of lobes per cell. G, Illustrations of cell area, cell perimeter, lobe aspect ratio, convex hull-fit, number of lobes per cell, and difference between true lobe and tricellular junction. Lobe aspect ratio in (F) is the ratio of depth/width of the lobe. Error bars = SE; 55 > n > 40 cells from six to eight seedlings for each measurement. Asterisks indicate statistically significant differences between wild-type and *any1* pavement cells of the same developmental stage ($P < 0.001$, Student's *t*-test). The mean lobe aspect ratio in (F) represents all the true lobes in the measured cells.
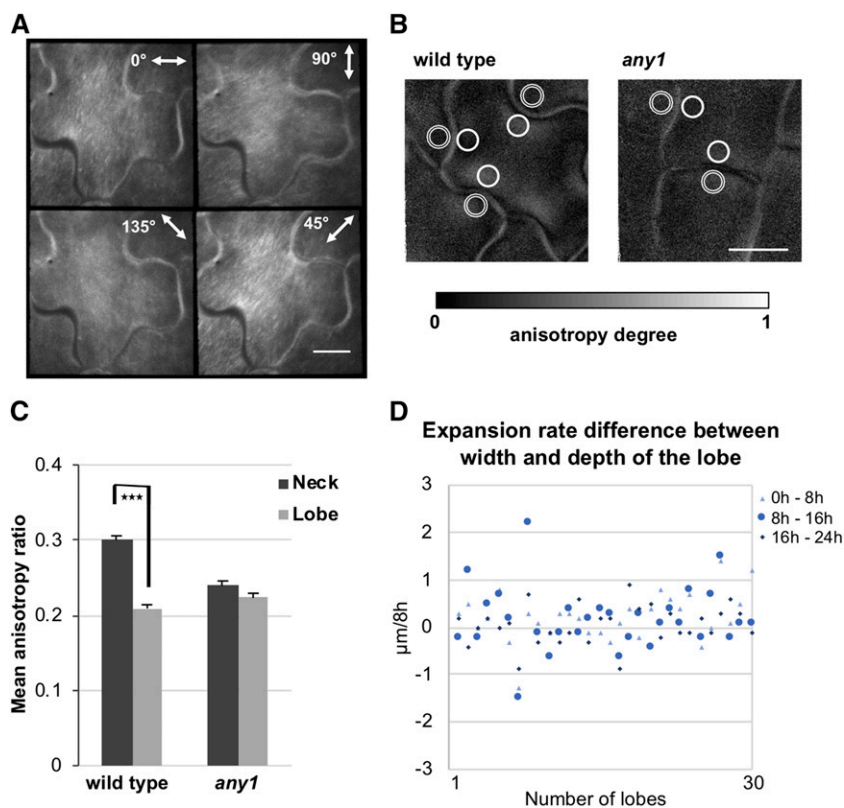
Figure 2. Cellulose alignment at the periclinal wall of wild-type and *any1* pavement cells. A, Fluorescence polarization at four different angles of cellulose microfibrils stained with S4B at 3 d after germination of wild-type pavement cells. B, Anisotropy degree of cellulose microfibrils represented by the pixel intensity at 1 d after germination of wild-type and *any1* cells. Double-lined circles (lobe regions) and solid-lined circles (neck regions) indicate examples of regions of interest used for the graph in (C). Scale bars = 10 μm. C, Anisotropy of cellulose alignment at the neck and the corresponding lobe regions of the wild type and *any1* mutant at 1 d after germination measured based on the signal intensity of each pixel at different emission angles. Error bars = SE. Asterisks indicate statistically significant differences ($P < 0.001$, paired *t* test). $n = 54$ necks and adjacent lobes of the same undulation. All necks from two or three cells taken from 13 and 16 seedlings for wild type and *any1*, respectively, were used in this analysis. D, Difference in the expansion rates between the width and the depth of the lobe at the early stages of lobe formation in the wild type. The same lobe was monitored over 24 h at 8 h intervals. The difference in expansion rates between the width and the depth of the lobe was calculated as $(width_{th} - width_{th-8h}) - (depth_{th} - depth_{th-8h})$. $n = 30$ lobes. All lobes from two cells from three different seedlings were used in the analysis.

early stages (1 d after germination) of pavement cell development (Fig. 2B) by using the anisotropy values of fluorescence polarization. The difference in average anisotropy degree between neck and the corresponding lobe regions was statistically significant in the wild-type pavement cells ($P < 0.0001$, paired *t* test) but not in *any1* cells ($P > 0.05$, paired *t* test; Fig. 2C). Given that *any1* mutants had lobes, albeit shallow, these results suggest that highly aligned cellulose microfibrils at the indentation side of the undulation are involved in augmenting lobe amplitude during differentiation but that the initiation of lobes does not seem to require a differential in the alignment of cellulose microfibrils.

The net-like configuration of cellulose microfibrils at the lobe region of the early stages in the wild type (Fig. 2C) suggests isotropic expansion of that region. We measured the expansion rate of the lobe depth and width of each lobe during the first 24 h of its development to assess the direction of the expansion. The

difference in the expansion rate between lobe width and lobe depth was close to zero (Fig. 2D). These results suggest that during the early stages, the periclinal wall in the lobe undergoes isotropic expansion, in agreement with observations of fiducial marker displacement reported by Armour et al. (2015).

Subcellular Variation in Periclinal Wall Stiffening Is Associated with Lobe Initiation and Subsequent Expansion

Sampathkumar et al. (2014) showed that the outer face of the periclinal wall in fully lobed cells exhibits fibrillar structures, presumably microfibrils, that were speculated to increase the local stiffness when probed with the orthogonally acting atomic force microscope. Our data indicate that enrichment of microfibrils at the neck side appears early during development and that

pectin may potentially cause an even earlier stiffness inhomogeneity, but the visual evidence of these polysaccharides does not provide proof of actual mechanical differentials. We therefore wanted to assess the stiffness of the cell wall material at undulations in *any1* and compare it to the wild type.

To map stiffness through the thickness of the wall rather than just at the outer face, we used Brillouin microscopy, an all-optical method that can be used to noninvasively characterize mechanical properties of biological materials (Scarcelli et al., 2015; Bidhendi and Geitmann, 2019b). It has, for example, been used successfully to characterize corneal biomechanics (Yun and Chernyak, 2018). The phenomenon of Brillouin scattering arises due to the interaction of an incident visible light (photons) with inherent sound waves (phonons) within the material. Generally, instrumentation comprises a Brillouin spectrometer and a standard inverted confocal microscope. As with any confocal modality, 3D mapping can be performed with high spatial resolution, dictated by the objective lens. The distance between the peaks of the Brillouin spectrum and the incident laser is the Brillouin Frequency Shift (BFS) and lies in the gigahertz frequency range. Inputting the index of refraction and density values of the measured material, the BFS can be converted to longitudinal modulus, the ratio of axial stress to axial strain in a constrained setting (Supplemental Note S1, Eq. 1). When comparing longitudinal modulus measured by the high-frequency Brillouin scattering with the traditional low-frequency Young's modulus, it is critical to note that these measures have large expected differences in magnitudes (gigapascals versus kilopascals). In recent years, several works have examined the correspondence between the BFS and longitudinal modulus with Young's modulus and found that these two moduli trend in the same direction with the underlying biophysical properties, and thus, within a given material, BFS could be used to extract relative information about modulus changes (Scarcelli and Yun, 2007; Scarcelli et al., 2011, 2015). The suitability of Brillouin technique for determining the stiffness of plant cell wall was addressed earlier by Elsayad et al. (2016). Further details of this technique are provided in Supplemental Notes S2 and S3 and Supplemental Figure S4.

Here, we observed that cellulose crystallinity contributes to the stiffness of the pavement cells. Firstly, we found that, when measured in the central regions of the periclinal walls, the Brillouin shift in the *any1* mutant displayed a significant decrease compared to the wild type ($P < 0.001$, Student's t test; Fig. 3, A and B). The reduction in the stiffness of the cell wall in the *any1* mutant was corroborated by performing a mechanical tensile test on the dark-grown hypocotyl of the wild type and the *any1* mutant. This mechanical tensile test revealed that the apparent Young's modulus of the dark-grown hypocotyl was reduced significantly in the *any1* mutant compared to the wild type (Supplemental Fig. S5). These results show that general reduction in cellulose crystallinity in the *any1* mutant causes reduction

in wall stiffness, and that the Brillouin technique is a reliable tool to noninvasively detect such change in the wall stiffness.

Secondly, the Brillouin shift revealed differences in stiffness at the lobe and the corresponding neck regions at an early stage of development (1 d after germination). Consistent with our previous findings, for both the neck and lobe regions, the BFS and longitudinal modulus of the wild type was significantly higher than that in the *any1* mutant ($P < 0.001$, Student's t test; Fig. 3, C and D). For the wild type, the neck had a significantly higher BFS and longitudinal modulus compared to the lobe region ($P < 0.0001$, paired t test; Fig. 3, C and D). This corroborates and expands on the information previously obtained on fully developed pavement cells using atomic force microscopy (Sampathkumar et al., 2014). Interestingly, a significant, albeit less substantially, elevated BFS and longitudinal modulus of the neck was found for the *any 1* mutant pavement cells ($P < 0.001$, paired t test; Fig. 3, C and D). These results suggest that the high degree of cellulose crystallinity translates to a stronger stiffness differential between neck and lobe in the wild type, which we hypothesize to promote the amplitude development of the lobe at later stages.

Cortical Microtubules Are Not Affected by the Reduction of Cellulose Crystallinity, and Their Localization Evolves during Lobe Formation

The hypothesized role of cellulose microfibrils during lobe formation arises from the observation of cortical microtubules at the periclinal wall of pavement cells (Szymanski, 2014; Bidhendi et al., 2019). The initiation of lobes involves the reconfiguration of a typically net-like configuration of the cortical microtubules to one that is aligned perpendicular or fan-like to the tangent of the neck region at the periclinal wall (Fu et al., 2005; Zhang et al., 2011; Armour et al., 2015; Higaki et al., 2017). We crossed *any1* with GFP:TUBULIN6 (TUB6) to examine whether the cortical microtubule organization is associated with the initiation of the undulation in the pavement cells of *any1*. The mean circularity and lobe number per cell of GFP:TUB6/*any1* pavement cells was similar to that of *any1* (Supplemental Fig. S6, A and B). The organization of microtubules in the epidermal cells of the leaf, hypocotyl, and roots is not affected in the *any1* mutant (Fujita et al., 2013). Moreover, the perpendicular bundles of cortical microtubules at the neck regions of the periclinal wall were not affected in *any1* pavement cells compared to the wild type (Supplemental Fig. S6C). We monitored the cortical microtubules and the changes in the cell wall of pavement cells in the wild type and *any1* mutant over 18 h with 6-h time-lapse intervals (Fig. 4, A–F). We quantitatively determined the alignment (i.e. degree of anisotropy) of cortical microtubules at the periclinal wall (Fig. 4, C and F). The anisotropy degree at the prospective neck region at time 0 was higher in both wild type and *any1* compared to the prospective
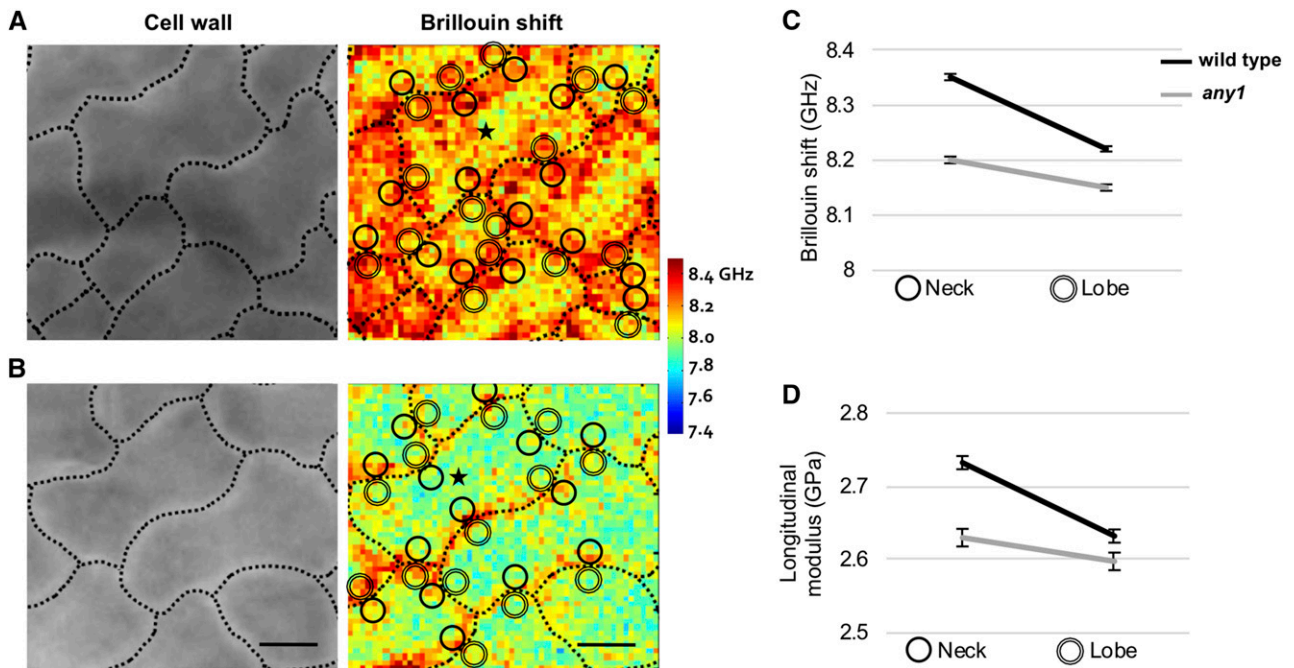
Figure 3. Mechanical stiffness of the periclinal wall of the wild-type and *any1* pavement cells assessed by Brillouin microscopy. A and B, Fluorescence micrograph (PI label, left) and Brillouin shift (stiffness map, right) of wild-type (A) and *any1* (B) pavement cells at 1 d after germination. The Brillouin shift is given in gigahertz and presented as a heatmap. In the micrographs, the dotted lines indicate cell outlines. Double-lined circles (lobe regions) and solid-lined circles (neck regions) indicate examples of regions of interest used for (C) and (D). Scale bars = 10 μm. Regions of interest = 9 μm^2 and pixel size = 1 μm^2. Asterisks indicate the central region of a cell where the Brillouin shift in the *any1* is significantly reduced compared to the wild type ($P < 0.001$, Student's t test). n = 25 cells for wild type and *any1*. C and D, The mean value of Brillouin shift (C) and the calculated longitudinal modulus (D) of the neck and the corresponding lobe regions in wild-type (black line) and *any1* (gray line) pavement cells. Error bars = SE. n = 40 necks and corresponding lobes of the same undulation. All necks from two or three cells from six seedlings for wild type and *any1* were used in this analysis.

lobe regions of the same undulation at the periclinal wall (Fig. 4G). To confirm the tight relation of cortical microtubule bundles with undulation formation, both GFP:TUB6 and GFP:TUB6/*any1* were grown in the presence of oryzalin, a herbicide that leads to the depolymerization of cortical microtubules (Supplemental Fig. S6C; Morejohn et al., 1987). In both lines, the mean lobe number was significantly reduced compared to the same developmental stage of the control pavement cells (Supplemental Fig. S6, D and E). This indicates that cortical microtubules in both wild type and *any1* mutant cells play a significant role in lobe development.

Demethyl-Esterified Pectin May Play a Role during Lobe Initiation and Is Localized at the Neck Regions

To answer how undulations are initiated at reduced cellulose crystallinity in the pavement cells of *any1*, we investigated the role of HG pectin in cell shaping. HGs are secreted in highly methylated form and can be modified in muro through the activity of PMEs. The degree of pectin esterification is known to control the cellular expansion in several biological systems (Chebli et al., 2012; Palin and Geitmann, 2012; Peaucelle et al.,

2015; Bou Daher et al., 2018). Demethyl-esterified pectin gelates by binding to calcium ions, which increases the stiffness of this polymer material in vitro (Ngouémazong et al., 2012) and in muro (Bou Daher et al., 2018). This polymer is associated with the neck region of Arabidopsis pavement cells (Bidhendi et al., 2019). We investigated the shape of pavement cells in several PME and PMEI mutants (Supplemental Fig. S7A) selected based on their expression levels in the cotyledon (Winter et al., 2007). Although several of the mutants (*pme3*, *pme44*, and *pmei41*) showed a significantly elevated number of lobes per cell (Supplemental Fig. S7A), the effect seemed to result from an increased overall growth rate of the cell rather than an increase in lobe initiation events because lobe period remained unaltered (Supplemental Fig. S7B).

Next, we wanted to test whether pectin plays a more prominent role when the crystallinity of cellulose is reduced. To examine this hypothesis, we grew the mutants in the presence of 1-cyclohexyl-5-(2,3,4,5,6-pentafluorophenoxyl)-1λ,2,4,6-thiatriazin-3-amine (CGA 325'615; CGA). This herbicide reduces cellulose crystallinity at picomolar concentrations and increases the relative abundance of amorphous cellulose (Peng et al., 2001). It has no significant effect on overall
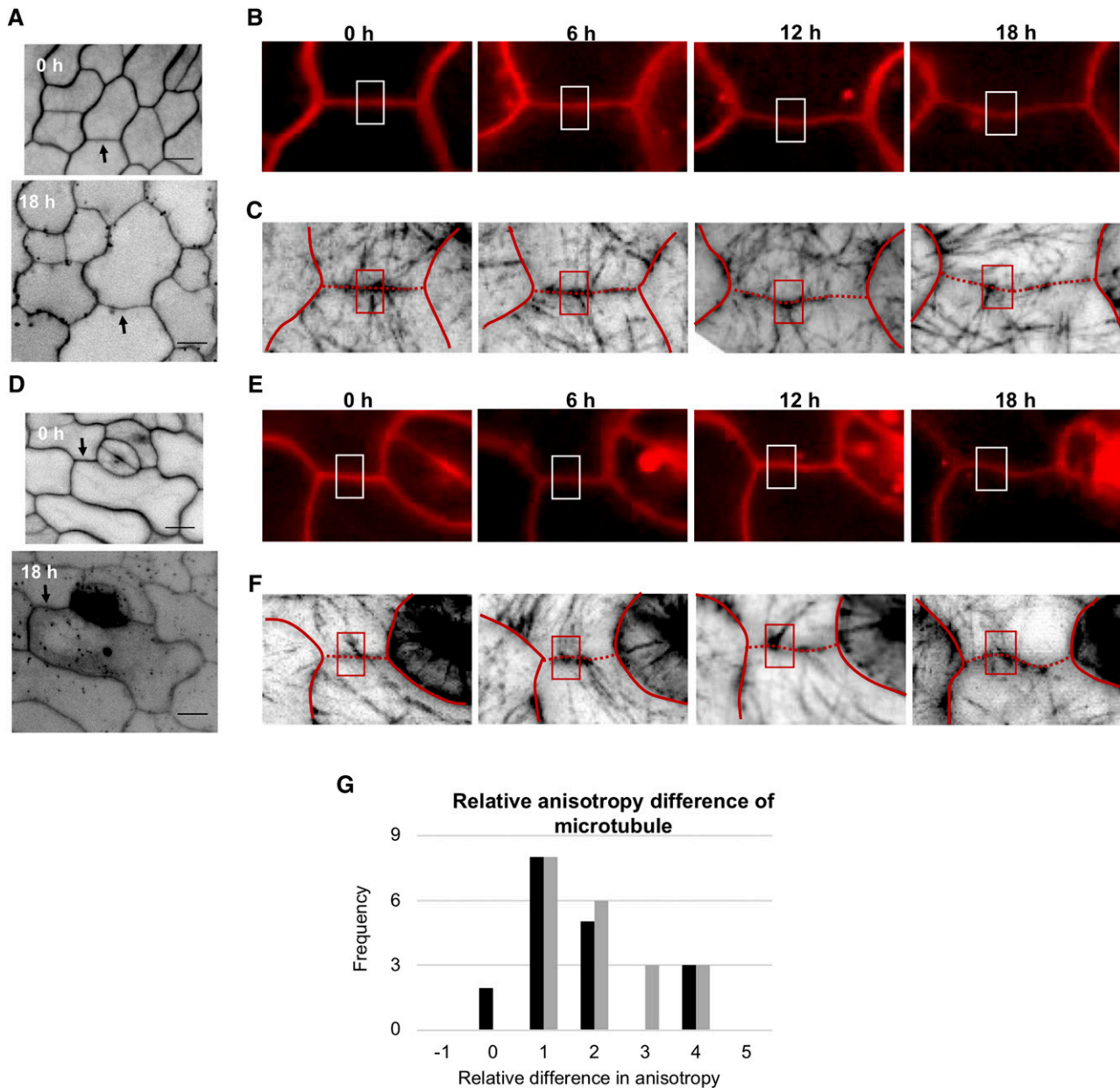
Figure 4. Arrangement of cortical microtubules during the development of undulations in wild-type and *any1* pavement cells expressing GFP:TUB6. A to F, Fluorescence micrographs of wild-type (A–C) and *any1* (D–F) pavement cells at 1 d after germination monitored over 18 h. The cell wall (stained with PI in A, B, D, and E) and cortical microtubules (GFP:TUB6, C and F) were visualized in 6-h time-lapse intervals. Arrows in (A) and (D) indicate the cell wall region that is represented in time-lapse images. Rectangles in (B) and (E) indicate the region on the anticlinal wall forming an undulation; (C) and (F) show the arrangement of cortical microtubules at the periclinal wall during the initiation and the development of the bend (rectangles). Red lines in (C) and (F) trace the anticlinal wall that is shown in (B) and (E), respectively. The dotted regions in (C) and (F) represents the anticlinal wall of interest. G, Frequency of the relative difference in cortical microtubule anisotropy between the prospective neck and the corresponding lobe of the same undulation at time 0 at the periclinal wall in GFP:TUB6 (black bars) and GFP:TUB6/*any1* (gray bars). *n* = 18 necks and 18 adjacent lobes from seven seedlings for GFP:TUB6 and 20 necks and 20 adjacent lobes from 11 seedlings for GFP:TUB6/*any1*. Scale bars = 10 μm.

cellulose content (Supplemental Fig. S8A). Moreover, it has no effect on the cytoskeleton and Golgi bodies (Crowell et al., 2009). Cellulose crystallinity was reduced significantly in the Arabidopsis cotyledons of the wild-type seedlings when they were grown in the presence of CGA compared to the control (Supplemental Fig. S8B). Moreover, the degree of cellulose crystallinity in the CGA-treated seedlings is comparable to that of

any1 (Supplemental Fig. S8B). The mean circularity and lobe number of pavement cells of the CGA-treated seedlings were similar to those of the *any1* mutant (Fig. 1, A–E; Supplemental Fig. S8, C–G). The orientation of cortical microtubules in the pavement cells was not altered under the effect of CGA compared to the wild type (Supplemental Fig. S8H). In the presence of the drug, pavement cells of *pmei37* showed a significantly reduced lobe period compared to the wild type (Fig. 5A; Supplemental Fig. S7, B and C). However, when the drug was present, neither in the wild type nor in the mutant did the aspect ratio of the lobes reach that of the respective untreated control (Fig. 5B). In the *pmei37* mutant treated with CGA, the percentage of esterification was significantly reduced compared to wild type in the presence of CGA (Supplemental Fig. S9, A and B).

Next, we investigated the localization of demethyl-esterified pectin in the *any1* mutant and compared it to the wild-type pavement cells. The localization of this polymer is connected with the neck side of the undulation in several angiosperms and in Arabidopsis pavement cells (Sotiriou et al., 2018; Bidhendi et al., 2019). We first attempted to identify the spatial localization of demethyl-esterified pectin at the periclinal wall using a specific monoclonal antibody (LM19). The antibody label revealed presence of the demethyl-esterified

pectin at the neck region in the wild-type and *any1* pavement cells. However, antibody label of the periclinal wall was of inferior quality as it was patchy (Supplemental Fig. S10), which prompted us to corroborate the evidence with different probes. We used COS[488], a molecular probe specific for demethyl-esterified pectin (Mravec et al., 2014), and compared the fluorescence intensity at the neck and the corresponding lobe of the same undulation. In the wild-type and *any1* pavement cells, demethyl-esterified pectin was enriched at the neck side. This difference was high in the early developmental stages in *any1* mutant cells, similar to wild-type cells (Fig. 5, C and D). Furthermore, we monitored the spatial pattern of demethyl-esterified pectin over time to determine the correspondence of its dynamics with that of cortical microtubules and changes in cell shape. Monitoring was conducted over 18 h with 6-h time-lapse intervals. We used propidium iodide (PI), a dye that is commonly used to stain cell walls and can be used to evaluate the esterification status of cell walls (Rounds et al., 2011). PI staining showed similar spatial patterns at the periclinal wall compared to the COS[488] probe (Fig. 6A). Quantitative determination of the changes in the abundance of demethyl-esterified pectin and the enrichment of cortical microtubules at prospective neck regions at the periclinal wall revealed that the former preceded the latter during the onset of curvature
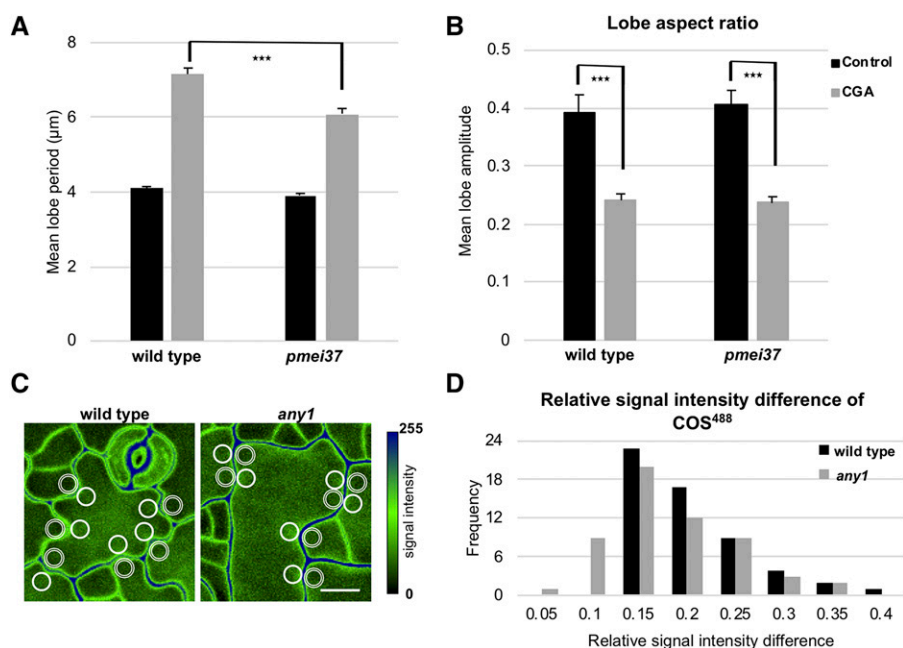
Figure 5. Role of demethyl-esterified pectin in the shaping of pavement cells. A and B, Mean lobe period (A) and mean lobe aspect ratio (B) in wild type and *pmei37* at 4 d after germination for control (DMSO; black bars) and seedlings grown in the presence of CGA (gray bars). Error bars = SE. 70 > *n* > 50 cells from 10 to 15 seedlings for each measurement for (A), and *n* = all lobes of 12 cells from eight seedlings for each measurement for (B). Asterisks indicate statistically significant differences (*P* < 0.001, Student's *t*-test). C, Fluorescence micrographs (maximum projection of z-stacks) of wild-type and *any1* pavement cells stained with COS[488] at 1 d after germination. Double-lined circles (lobe regions) and solid-lined circles (neck regions) indicate examples of regions of interest used in (D) to calculate the abundance of demethylated pectin at lobe/neck pairs. Scale bar = 10 µm. D, Distribution of the relative differences in the signal intensity of COS[488] between the neck and the corresponding lobe of the same undulation. *n* = 56 necks and 56 corresponding lobes from seven seedlings for wild type and *any1*.

formation (Fig. 6, B–H; Supplemental Fig. S11). These results support the notion that demethyl-esterified pectin in the wall of a pavement cell plays a major role in lobe initiation.

DISCUSSION

In this study, we asked how the cell wall regulates the developmental process of the undulation formation in the epidermal pavement cells of Arabidopsis. Our results are consistent with the concept of a two-step mechanism consisting of distinct and differently regulated processes: initiation and subsequent expansion (Fig. 7). The initiation step involves an increase in the stiffness of the periclinal wall at the prospective neck side of the undulation through a local accumulation of demethyl-esterified pectin. The subsequent expansion is controlled by the gradual enrichment in cellulose microfibrils aligned perpendicularly to the tangent of the neck side of the undulation.

Cellulose microfibrils have been suggested to control both the initiation and the subsequent expansion of the undulation because of their high tensile strength along their long axis (Kerstens et al., 2001; Suslov and Verbelen, 2006). We show that cellulose crystallinity is associated with the stiffness of the cell wall, with higher stiffness characterizing a higher crystallinity ratio. The increase in the circularity of the *any1* mutant pavement cells was associated with a reduction in cellulose

Figure 6. Temporal association between the dynamics of demethyl-esterified pectin and cortical microtubules at developing cell border curvatures. A, Fluorescence micrograph (maximum projection of z-stack) of pavement cells stained with PI of wild type at 1 d after germination. Arrows indicate local enrichment in PI label at the neck regions of developed cell border curvatures. B, Relative differences in the signal intensity of PI (red) and GFP:TUB6 (green) label between prospective necks and adjacent regions at the periclinal wall at times 0 and 6 h. n = 17 prospective neck regions from three seedlings. Error bars = SE. At time 0, all measured cell border regions were straight, whereas at 6 h they showed slight but discernible curvature. C, Evolution of curvature (calculated as reciprocal of its radius) in the two cell border regions indicated in (D), (E), (F), (G), and (H) over a 18-h observation period. Black dashed and solid lines represent the cell border segments identified by white dashed and solid rectangles in (F), (G), and (H), respectively. The black/white dashed line/rectangle indicates a cell border segment that is already curved at time 0, whereas the black/white solid line/rectangle identifies a cell border segment that is straight at time 0 and develops a curvature by 18 h. D to H, Fluorescence micrographs of wild-type epidermis monitored over 18 h and visualized in 6-h time-lapse intervals. D, Maximum projections of z-stacks of sample shown in (E), (F), and (H), stained with PI. E, Single optical sections of sample shown in (D), showing the anticlinal wall stained with PI over time. Arrows in (D) and (E) indicate two cell border segments monitored in the time-lapse series (upward pointing arrow, curvature present at time 0; downward pointing arrow, straight at time 0). F, Maximum projections of z-stacks showing PI signal for demethyl-esterified pectin. G, Maximum projections of z-stacks showing cortical microtubules at the periclinal wall (GFP:TUB6). H, Merge of the PI and the GFP:TUB6 signals. White lines in (F) and (H) and red line in (G) trace the anticlinal wall that is shown in (E). The dotted regions of the white lines in (F), (G), and (H) represent the anticlinal wall of interest. Scale bars = 10 μm.
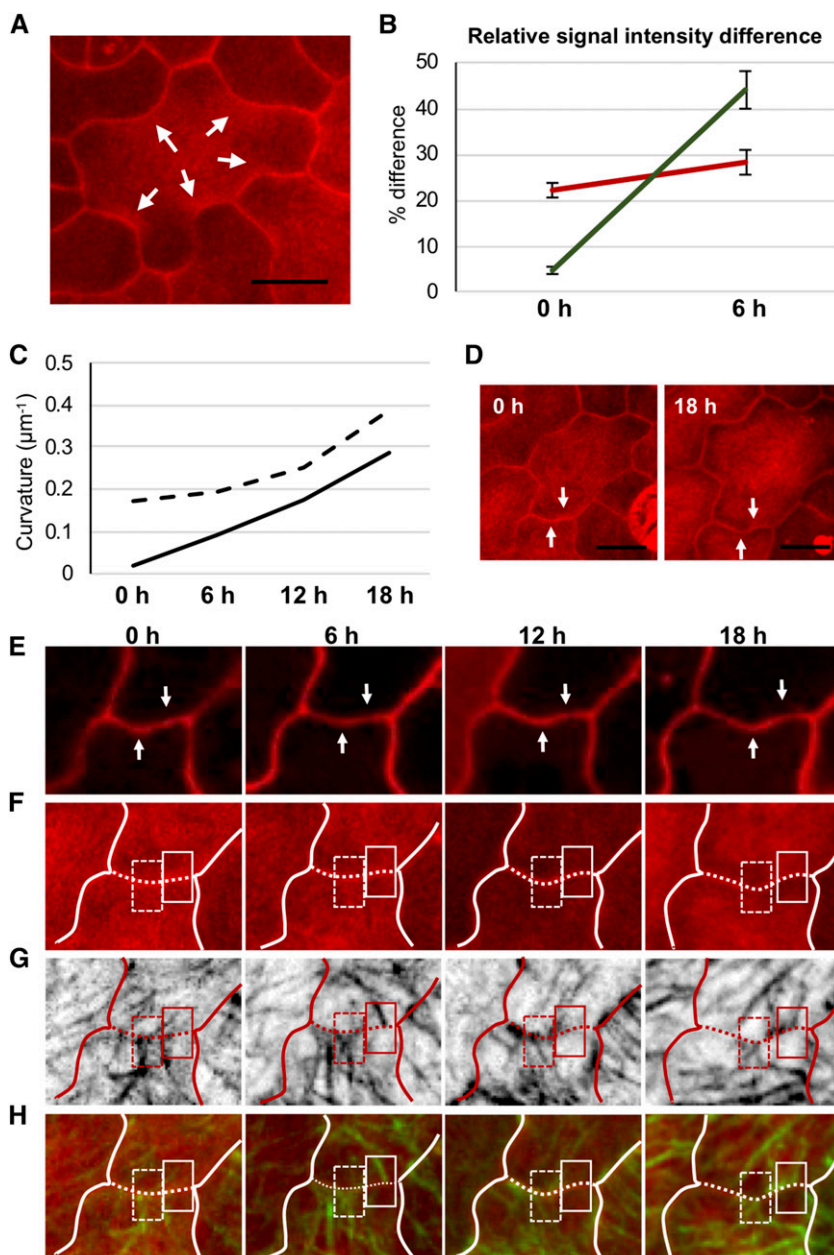
crystallinity and, thus, a swelling phenotype (Fujita et al., 2013). However, pavement cells of *any1* were still able to restrict the expansion at specific spatial regions and initiate undulations. We hypothesized that this might result from a subcellular difference in the arrangement of cellulose microfibrils at the neck/lobe regions as shown previously (Panteris et al., 1994; Panteris and Galatis, 2005; Sampathkumar et al., 2014). At early stages of lobe formation in the wild type, the anisotropy degree of cellulose microfibrils increased at the neck side compared to the lobe side of an undulation. This accumulation of cellulose was associated with an increase in lobe depth during subsequent cell development. We posit that this association is causal because in the *any1* mutant the difference in anisotropy degree at the two opposing sides of the undulation was smaller than in the wild type, and, consistent with that, lobe depth did not augment significantly during subsequent cell development. Given that *any1* mutants are capable of initiating lobes and this initiation was not associated with a marked difference in the cellulose anisotropy between opposing sides of the undulation, we conclude that high crystallinity and the perpendicular orientation of cellulose microfibrils coincide primarily with depth augmentation of the lobe, more than with the initiation process of the lobe. We speculate that the increased lobe period in the *any1* pavement cells might be a consequence of the inability of the cells to stabilize initiated lobes. Many barely initiated lobes may be straightened during further growth of the cell unless robustly stabilized by cellulose enrichment in the neck.
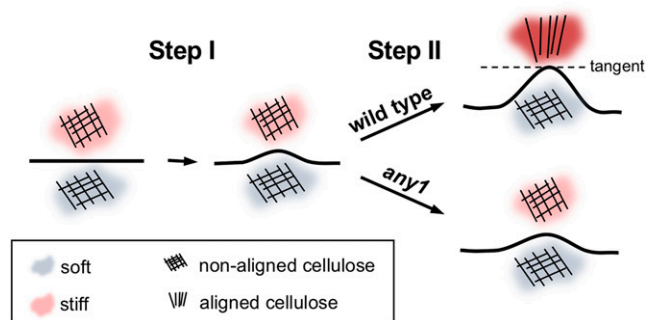
Figure 7. Proposed two-step mechanism for undulation formation during the development of pavement cells. In Step I, an increase in the wall stiffness at a prospective neck region is generated through localized enrichment in demethylated pectin. The increased stiffness at the prospective neck side of the undulation leads to differential expansion of the periclinal wall during cell growth with the neck side expanding less than the opposing lobe side. The resulting symmetry break and stiffness differential generate a local elevation of stress (Sampathkumar et al., 2014; Bidhendi et al., 2019), which in turn attracts accumulation of microtubules at the neck (Hamant et al., 2008), resulting in deposition of cellulose, and by consequence, an augmentation of lobe expansion through a feedback loop (Step II). This feedback-driven augmentation of lobe depth is absent in the *any1* mutant, where cellulose crystallinity and alignment are low.

The orientation of cellulose microfibrils at the neck and the lobe sides in the wild type suggests that these periclinal wall regions resist turgor-driven expansion differently. Upon lobe initiation, expansion at the lobe region may be isotropic, whereas expansion at the neck region is much reduced and primarily parallel to the tangent of the lobe as suggested by the displacement of fiducial markers (Armour et al., 2015). During lobe expansion, the periclinal wall in the lobe seems to undergo anisotropic expansion as reported by Elsner et al. (2018), likely promoted by the transverse alignment of cellulose microfibrils at the base of the lobe perpendicular to its long axis (Sampathkumar et al., 2014; Bidhendi et al., 2019).

The spatial stiffness map of the periclinal wall reflects the mechanism that leads to the formation of the undulation in the wild type and *any1* mutant. The stiffness at the cell periphery of the periclinal wall, at the early developmental stages, varies with the material at the neck being stiffer compared to the lobe regions in the wild type. This explains the low expansion rate at the prospective neck side of the undulation compared to the lobe side, as suggested by Armour et al. (2015) and Bidhendi et al. (2019). The higher stiffness value at the neck region of the wild type is in agreement with the reported stiffness of the neck regions at the late stages of pavement cell development that is measured by atomic force microscopy (Sampathkumar et al., 2014). Also, the elevated stiffness at necks is associated with the presence of both higher degree of cellulose crystallinity and high anisotropy ratio of cellulose in the wild type. The presence of cortical microtubules and cellulose microfibrils extending from the periclinal wall into the depth of the anticlinal wall (Zhang et al., 2011; Belteton et al., 2018; Bidhendi et al., 2019) suggests that cell wall stiffness on the neck side extends into the depth of the anticlinal wall, although we did not show this here. While this would be consistent with most studies, it is difficult to reconcile with the concept by Majda et al. (2017), who proposed that the neck side of the anticlinal wall is softer than the lobe side. A possible explanation could be that atomic force microscopy is more sensitive to other wall polymers when probing parallel to the direction of the cellulose microfibrils, but additional research is clearly warranted.

Remarkably, in the *any1* mutant pavement cells, a small difference in the stiffness between the two opposing sides of the undulation was detected in the initial developmental stages. This raises the question of the biochemical underpinning of this differential. We speculated that the relative quantities of amorphous cellulose at the opposing sides of the bend are different, or that other strengthening polymers at the neck regions are involved. We suspected demethyl-esterified pectin to play a role, as suggested by Bidhendi et al. (2019), and consistent with this, the *pmei37* mutant showed a reduction in lobe period under conditions of pharmacologically reduced cellulose crystallinity. Satisfactory labeling quality of demethyl-esterified pectin at the periclinal wall using a specific antibody

was elusive, but complementing evidence based on COS[488] label revealed clear enrichment of this polymer at the neck regions compared to the lobe regions in both wild-type and *any1* mutant cells. The association of this polymer with the stiffness of the wall and, therefore, the restriction of the expansion can be due to the ability of this polymer to form gelation in the presence of calcium ions (Ngouémazong et al., 2012). The spatially confined enrichment of this polymer is associated with stiffer regions in the pollen tube (Zerzour et al., 2009; Chebli et al., 2012). Overexpression of PME5 increases the stiffness of the wall in the etiolated hypocotyl (Bou Daher et al., 2018). Moreover, increasing the demethyl esterification of the wall can restrict the growth and the expansion of the wall as shown in the pollen tube and elongated shoot cells (Bosch et al., 2005; Derbyshire et al., 2007). Therefore, demethyl-esterified pectin may play a significant role by increasing the stiffness of the periclinal wall at prospective neck regions leading to the initiation of an undulation. This process also changes the stress distribution at the periclinal wall that plays an important role during lobe formation because it regulates, in a feedback mechanism, the arrangement of cortical microtubules and the auxin-Rho-GTPase signaling pathway that has been proposed to control pavement cell development (Fu et al., 2005; Hamant et al., 2008; Jacques et al., 2013; Sampathkumar et al., 2014; Bidhendi et al., 2019).

The suggested role of cellulose microfibrils in the initiation of the undulation was based on the observation that cortical microtubules are oriented perpendicular or fan-like to the tangent of the neck region at the periclinal wall of mature pavement cells (Zhang et al., 2011; Sampathkumar et al., 2014). Armour et al. (2015) showed that cortical microtubules at the periclinal wall are present at the prospective neck regions in wild-type pavement cells (Armour et al., 2015). We show that this microtubule configuration applies equally to the *any1* mutant pavement cells in which cellulose crystallinity is known to be reduced and the alignment of cellulose is more random. Additionally, when wild-type and *any1* mutant seedlings were grown in the presence of oryzalin, pavement cells failed to expand lobes. Based on these results, we propose that the early accumulation of cortical microtubules may be the result of a locally confined increase in stress caused by the presence of demethyl-esterified pectin and a resulting stiffening of the wall and lobe initiation. Cellulose microfibrils are important primarily for the second developmental step, the augmentation of lobe depth.

The advantage of the two-step mechanism over concepts that suggest the initiation of undulations based on cellulose microfibrils is that it can explain how pavement cells are able to initiate new neck regions during the developmental process not only in straight walls but also within existing lobes where the orientation of cellulose is more random. This is supported by the observation of mutation in PMEI that allowed initiation of new lobes when cellulose crystallinity was reduced. The demethylation process of the esterified

pectin at the existing lobe region can increase the stiffness and therefore the stress that subsequently results in increased local bundling of cortical microtubules (Hamant et al., 2008; Jacques et al., 2013).

MATERIALS AND METHODS

Plant Materials

Arabidopsis (*Arabidopsis thaliana*) wild-type (ecotype Columbia-0), GFP-TUB6 (accession no.; CS6550), *pme1* (AT1G53840; SALK_120021), *pme3* (AT3G14310; CS2103492), *pme15* (AT2G36710; CS859505), *pme25* (AT3G10720; SALK_021426C), *pme44* (AT4G33220; CS837906), *pmei37* (AT3G47670; SALK_068827C), and *pmei41* (AT3G62820; SALK_027168C) seeds were obtained from the Arabidopsis Biological Resource Center. The *any1* mutant seeds were obtained from the lab of Dr. Geoffrey Wasteneys (University of British Columbia, Canada; Fujita et al., 2013). The *any1*/GFP-TUB6 was obtained by crossing plants expressing p35S::GFP-TUB6 with *any1* plants, and F2 progeny expressing GFP-TUB6/*any1* were used for visualizing microtubules. Transfer DNA insertions were confirmed by PCR from genomic DNA with the following LP/RP primer pairs: 5′-TCAGTTTATTGGTGGTGGAGG-3′ and 5′-TCGATCAGATCTCCACAAACC-3′ for *pme1*, 5′-AATTGGTTGAAT GACGAAACG-3′ and 5′-TACGTACCTGCCCCTTCAAC-3′ for *pme3*, 5′-TGG ATTCTATGGGGCTCAAG-3′ and 5′-TTTATGGGAGAGCCATGGAC-3′ for *pme15*, 5′-GCGTAATCGACAAAGTGACG-3′ and 5′-ACTCAGCTCCGATAA CTCGC-3′ for *pme25*, 5′-AGCAACCAGTTTCACAAACG-3′ and 5′-CTTTTG TACCAGCGAAACCC-3′ for *pme44*, 5′-TGTGGTCTACCGTTTTCACG-3′ and 5′-TCACTATGCTCCGTGACTCG-3′ for *pmei37*, and 5′-ACCAACGAATTG TTATCGGC-3′ and 5′-TACTCGTTAGGTGGCATGGG-3′ for *pmei41*.

Seeds were sterilized and kept at 4°C in the dark for 2 d. Seeds were grown in plates containing 0.5× Murashige and Skoog (MS; Thermo Fisher Scientific) salt, 1% (w/v) Suc, and 0.8% (w/v) plant agar (Sigma-Aldrich). The germination condition was 22°C under 8-h/16-h dark/light cycle.

The abaxial side of the cotyledon was used in this study. Images were taken from the midsection of the cotyledon (Supplemental Fig. S1). For image acquisition, samples were mounted between slide and coverslip for imaging. For time-lapse imaging, samples were placed immediately back in the in vitro growth chamber after each image acquisition.

Labeling Methods

For cellulose labeling, the seed coat was removed 18–22 h after germination to allow the penetration of the dye into the cotyledon of the wild-type and the *any1* mutant cells. The living seedlings were placed in 1.5-mL microcentrifuge tubes containing 0.02% (w/v) S4B (Sigma-Aldrich) in liquid 0.5× MS medium and 1% (w/v) Suc for 3 h at dark condition, then samples were washed three times with liquid 0.5× MS medium before observation. To allow observing cellulose microfibrils at 3 d after germination pavement cells, the cotyledons were brushed before applying the dye.

To label demethyl-esterified pectin, we used both a molecular probe (COS[488]) and immunolabeling (monoclonal antibody LM19) on 1-d–old seedlings of wild type and *any1*. For COS[488] label, living seedlings were placed in 1 μL/mL of the dye for 20 min and washed several times before observation in distilled water. For immunolabeling, seedlings were fixed with freshly prepared 3.5% formaldehyde in phosphate buffered saline (PBS; 135-mM NaCl, 6.5-mM Na$_2$HPO$_4$, 2.7-mM KCl, and 1.5-mM KH$_2$PO$_4$ at pH 7.3) and 1% Triton for 2.5 h followed by three washes with PBS buffer. Next, seedlings were washed three times with 2.5% (w/v) bovine serum albumin (BSA) in PBS buffer. The first antibody (LM19, rat IgM; PlantProbes) was diluted (1:50) in the BSA-BPS buffer and 1% Triton. Seedlings were incubated in the first antibody for 2.5 h. For controls, either the primary or the secondary antibody were excluded. Seedlings were washed three times with the BSA-BPS buffer after applying the first and the second antibody. The secondary antibody (Alexa Fluor 594 anti-mouse IgG; PlantProbes) was diluted 1:100 in the BSA-BPS buffer and 1% Triton. Seedlings were incubated in the secondary antibody for 2.5 h.

For cell shape metrics analysis and time-lapse imaging, cell walls were labeled with 0.01-mg/mL PI (Sigma-Aldrich) for 20 min, followed by three washes with distilled water before observation. For time-lapse imaging, labeling was applied at each time point before the observation.

Drug Treatments

Oryzalin (Riedel-de-Haën) was used to depolymerize the cortical microtubules. The final working concentration was 10 μM (stock concentration was 10 mM dissolved in dimethylsulfoxide [DMSO]; Sigma-Aldrich). The same volume of DMSO (v/v) was used for the control experiment. Seedlings were grown in a solidified 0.5× MS medium in the presence of the drug. CGA (CGA 325'615; Syngenta) was used to reduce cellulose crystallinity. The final working concentration was 0.9 nM (prepared from a 10-μM stock solution dissolved in DMSO). The same volume of DMSO (v/v) was used for the control experiment.

Measurement of Cellulose and Pectin Contents

Arabidopsis seedlings (4 d after germination) were fixed in 100% methanol for 4 h. Methanol was substituted with 100% ethanol and samples were critical-point–dried using a model no. EM CPD300 Critical Point Dryer (Leica). The epidermal surface composition was analyzed using Fourier-transform infrared spectroscopy-attenuated total reflection (FTIR-ATR) at the midinfrared beamline at the Canadian Light Source synchrotron (Lahlali et al., 2014). The globar source was employed as the infrared source. This ATR method used a germanium crystal (angle of incidence of 45°) attached to a Cary 600 Series FTIR Spectrometer (Agilent). Each infrared spectrum was recorded in the midinfrared range of 4,000–800 cm^{-1} wavenumbers at a spectral resolution of 4 cm^{-1}.

The data were analyzed with the software Orange 3.14 (https://github.com/biolab/orange3). The data were corrected by performing a baseline correction ("Rubber band") and by subtracting the background. The data were then normalized using the vector normalization algorithm, and a Gaussian smoothing of seven points was applied. The corrected data were transferred into the second derivative form by using the Savitzky–Golay algorithm. The estimation of components was determined by integrating the area between the baseline and specific band for cellulose (1,170–1,140 cm^{-1}), total pectin (1,270–1,215 cm^{-1}), and esterified pectin (1,763–1,723 cm^{-1}).

Measurement of Cellulose Crystallinity

A model no. D8 Discovery X-Ray Diffractometer (Bruker) was used to detect the amount of crystalline cellulose in the cotyledons of Arabidopsis. A Cu-source generated x-rays at 40 kV and 40 mA. The diffraction intensity was collected at the range of 4° to 60° with 0.005° steps. The intensity data from 5° to 40° in the 2-theta angle range were used in the analysis. Cotyledons were critical-point–dried and flattened before the measurement. The amount of crystalline cellulose was measured using the curve-fitting method assessed by the software DIFFRAC.EVA (Bruker AXS).

Microscopy and Image Acquisition

The spatial arrangement of cellulose microfibrils was visualized by Instantaneous FluoPolScope (Mehta et al., 2016; Swaminathan et al., 2017). Cell wall stiffness was measured by Brillouin microscopy (Scarcelli and Yun, 2007, 2011). The dynamic of cortical microtubules and the spatial distribution of demethylated pectin were visualized by model no. LSM 510 META/LSM 5LIVE/Axiovert 200M (Zeiss). A thorough description of the image acquisition and the methods used in data analysis is given in the Supplemental Materials and Methods.

Accession Numbers

Genome Initiative locus identifiers of the genes used in this article are as follows: At4g32410 (*any1*), AT1G53840 (*pme1*), AT3G14310 (*pme3*), AT2G36710 (*pme15*), AT3G10720 (*pme25*), AT4G33220 (*pme44*), AT3G47670 (*pmei37*), and AT3G62820 (*pmei41*).

Supplemental Data

The following supplemental materials are available.

Supplemental Note S1. Distinction between true lobes and tricellular junctions.

Supplemental Note S2. Calculating the longitudinal modulus.

Supplemental Note S3. Effect of cell geometry on the detected BFS.

Supplemental Materials and Methods. Microscopy and image acquisition, Image analysis and Method of tensile testing of hypocotyls.

Supplemental Figure S1. Region on the cotyledon used in this study.

Supplemental Figure S2. Difference between true lobe and tricellular junction.

Supplemental Figure S3. Fluorescence polarization of S4B dye reflects the anisotropy degree of cellulose.

Supplemental Figure S4. Effect of pavement cell geometry on Brillouin signal intensity and BFS.

Supplemental Figure S5. Apparent Young's modulus of hypocotyls measured using tensile test.

Supplemental Figure S6. Shape analysis of GFP:TUB6 and GFP:TUB6/*any1* pavement cells.

Supplemental Figure S7. Shape analysis of Arabidopsis wild-type, PME, and PMEI mutant pavement cells.

Supplemental Figure S8. Cellulose content and shape analysis of pavement cells under CGA treatment.

Supplemental Figure S9. Pectin content and percentage of esterified pectin in wild type and *pmei37* obtained using ATR spectroscopy.

Supplemental Figure S10. Spatial arrangement of demethyl-esterified pectin in the pavement cells of wild type and *any1* detected by monoclonal antibody.

Supplemental Figure S11. Image analysis of pectin and microtubule dynamics during time-lapse monitoring.

LITERATURE CITED

Altartouri B, Geitmann A (2015) Understanding plant cell morphogenesis requires real-time monitoring of cell wall polymers. Curr Opin Plant Biol **23:** 76–82

Anderson CT, Carroll A, Akhmetova L, Somerville C (2010) Real-time imaging of cellulose reorientation during cell wall expansion in Arabidopsis roots. Plant Physiol **152:** 787–796

Aouar L, Chebli Y, Geitmann A (2010) Morphogenesis of complex plant cell shapes: The mechanical role of crystalline cellulose in growing pollen tubes. Sex Plant Reprod **23:** 15–27

Armour WJ, Barton DA, Law AM, Overall RL (2015) Differential growth in periclinal and anticlinal walls during lobe formation in Arabidopsis cotyledon pavement cells. Plant Cell **27:** 2484–2500

Belteton SA, Sawchuk MG, Donohoe BS, Scarpella E, Szymanski DB (2018) Reassessing the roles of PIN proteins and anticlinal microtubules during pavement cell morphogenesis. Plant Physiol **176:** 432–449

Bidhendi AJ, Geitmann A (2019a) Geometrical details matter for mechanical modeling of cell morphogenesis. Dev Cell **50:** 117–125

Bidhendi AJ, Geitmann A (2019b) Methods to quantify primary plant cell wall mechanics. J Exp Bot **70:** 3615–3648

Bidhendi AJ, Altartouri B, Gosselin FP, Geitmann A (2019) Mechanical stress initiates and sustains the morphogenesis of wavy leaf epidermal cells. Cell Rep **28:** 1237–1250

Bosch M, Cheung AY, Hepler PK (2005) Pectin methylesterase, a regulator of pollen tube growth. Plant Physiol **138:** 1334–1346

Bou Daher F, Chen Y, Bozorg B, Clough J, Jönsson H, Braybrook SA (2018) Anisotropic growth is achieved through the additive mechanical effect of material anisotropy and elastic asymmetry. eLife 7: e38161

Chebli Y, Kaneda M, Zerzour R, Geitmann A (2012) The cell wall of the Arabidopsis pollen tube—spatial distribution, recycling, and network formation of polysaccharides. Plant Physiol 160: 1940–1955

Cosgrove DJ (1998) Cell wall loosening by expansins. Plant Physiol 118: 333–339

Cosgrove DJ (2014) Re-constructing our models of cellulose and primary cell wall assembly. Curr Opin Plant Biol 22: 122–131

Cosgrove DJ (2016) Plant cell wall extensibility: Connecting plant cell growth with cell wall structure, mechanics, and the action of wall-modifying enzymes. J Exp Bot 67: 463–476

Crowell EF, Bischoff V, Desprez T, Rolland A, Stierhof YD, Schumacher K, Gonneau M, Höfte H, Vernhettes S (2009) Pausing of Golgi bodies on microtubules regulates secretion of cellulose synthase complexes in Arabidopsis. Plant Cell 21: 1141–1154

Derbyshire P, McCann MC, Roberts K (2007) Restricted cell elongation in Arabidopsis hypocotyls is associated with a reduced average pectin esterification level. BMC Plant Biol 7: 31

Diddens I, Murphy B, Krisch M, Müller M (2008) Anisotropic elastic properties of cellulose measured using inelastic x-ray scattering. Macromolecules 41: 9755–9759

Eichhorn S, Young R (2001) The Young's modulus of a microcrystalline cellulose. Cellulose 8: 197–207

Elsayad K, Werner S, Gallemí M, Kong J, Sánchez Guajardo ER, Zhang L, Jaillais Y, Greb T, Belkhadir Y (2016) Mapping the subcellular mechanical properties of live cells in tissues with fluorescence emission-Brillouin imaging. Sci Signal 9: rs5

Elsner J, Lipowczan M, Kwiatkowska D (2018) Differential growth of pavement cells of *Arabidopsis thaliana* leaf epidermis as revealed by microbead labeling. Am J Bot 105: 257–265

Eng RC, Sampathkumar A (2018) Getting into shape: The mechanics behind plant morphogenesis. Curr Opin Plant Biol 46: 25–31

Fayant P, Girlanda O, Chebli Y, Aubin CE, Villemure I, Geitmann A (2010) Finite element model of polar growth in pollen tubes. Plant Cell 22: 2579–2593

Fu Y, Gu Y, Zheng Z, Wasteneys G, Yang Z (2005) Arabidopsis interdigitating cell growth requires two antagonistic pathways with opposing action on cell morphogenesis. Cell 120: 687–700

Fujita M, Himmelspach R, Ward J, Whittington A, Hasenbein N, Liu C, Truong TT, Galway ME, Mansfield SD, Hocart CH, et al (2013) The anisotropy1 D604N mutation in the Arabidopsis cellulose synthase1 catalytic domain reduces cell wall crystallinity and the velocity of cellulose synthase complexes. Plant Physiol 162: 74–85

Hamant O, Heisler MG, Jönsson H, Krupinski P, Uyttewaal M, Bokov P, Corson F, Sahlin P, Boudaoud A, Meyerowitz EM, et al (2008) Developmental patterning by mechanical signals in Arabidopsis. Science 322: 1650–1655

Higaki T, Takigawa-Imamura H, Akita K, Kutsuna N, Kobayashi R, Hasezawa S, Miura T (2017) Exogenous cellulase switches cell interdigitation to cell elongation in an RIC1-dependent manner in *Arabidopsis thaliana* cotyledon pavement cells. Plant Cell Physiol 58: 106–119

Jacques E, Verbelen JP, Vissenberg K (2013) Mechanical stress in Arabidopsis leaves orients microtubules in a 'continuous' supracellular pattern. BMC Plant Biol 13: 163

Kerstens S, Decraemer WF, Verbelen JP (2001) Cell walls at the plant surface behave mechanically like fiber-reinforced composite materials. Plant Physiol 127: 381–385

Kotzer A, Wasteneys G (2006) Mechanisms behind the puzzle: Microtubule–microfilament cross-talk in pavement cell formation. Botany 84: 594–603

Lahlali R, Jiang Y, Kumar S, Karunakaran C, Liu X, Borondics F, Hallin E, Bueckert R (2014) ATR-FTIR spectroscopy reveals involvement of lipids and proteins of intact pea pollen grains to heat stress tolerance. Front Plant Sci 5: 747

Majda M, Grones P, Sintorn IM, Vain T, Milani P, Krupinski P, Zagorska-Marek B, Viotti C, Jonsson H, Mellerowicz EJ, et al (2017) Mechanochemical polarization of contiguous cell walls shapes plant pavement cells. Dev Cell 43: 290–304

Majda M, Krupinski P, Jönsson H, Hamant O, Robert S (2019) Mechanical asymmetry of the cell wall predicts changes in pavement cell geometry. Dev Cell 50: 9–10

Mehta SB, McQuilken M, La Riviere PJ, Occhipinti P, Verma A, Oldenbourg R, Gladfelter AS, Tani T (2016) Dissection of molecular assembly dynamics by tracking orientation and position of single molecules in live cells. Proc Natl Acad Sci USA 113: E6352–E6361

Morejohn LC, Bureau TE, Molè-Bajer J, Bajer AS, Fosket DE (1987) Oryzalin, a dinitroaniline herbicide, binds to plant tubulin and inhibits microtubule polymerization in vitro. Planta 172: 252–264

Mravec J, Kračun SK, Rydahl MG, Westereng B, Miart F, Clausen MH, Fangel JU, Daugaard M, Van Cutsem P, De Fine Licht HH, et al (2014) Tracking developmentally regulated post-synthetic processing of homogalacturonan and chitin using reciprocal oligosaccharide probes. Development 141: 4841–4850

Ngouémazong DE, Jolie RP, Cardinaels R, Fraeye I, Van Loey A, Moldenaers P, Hendrickx M (2012) Stiffness of Ca^{2+}-pectin gels: Combined effects of degree and pattern of methylesterification for various Ca^{2+} concentrations. Carbohydr Res 348: 69–76

Palin R, Geitmann A (2012) The role of pectin in plant morphogenesis. Biosystems 109: 397–402

Panteris E, Galatis B (2005) The morphogenesis of lobed plant cells in the mesophyll and epidermis: organization and distinct roles of cortical microtubules and actin filaments. New Phytol 167: 721–732

Panteris E, Apostolakos P, Galatis B (1994) Sinuous ordinary epidermal cells: Behind several patterns of waviness, a common morphogenetic mechanism. New Phytol 127: 771–780

Peaucelle A, Wightman R, Höfte H (2015) The control of growth symmetry breaking in the Arabidopsis hypocotyl. Curr Biol 25: 1746–1752

Peng L, Xiang F, Roberts E, Kawagoe Y, Greve LC, Kreuz K, Delmer DP (2001) The experimental herbicide CGA 325'615 inhibits synthesis of crystalline cellulose and causes accumulation of non-crystalline beta-1,4-glucan associated with CesA protein. Plant Physiol 126: 981–992

Rounds CM, Lubeck E, Hepler PK, Winship LJ (2011) Propidium iodide competes with Ca^{2+} to label pectin in pollen tubes and Arabidopsis root hairs. Plant Physiol 157: 175–187

Sampathkumar A, Krupinski P, Wightman R, Milani P, Berquand A, Boudaoud A, Hamant O, Jönsson H, Meyerowitz EM (2014) Subcellular and supracellular mechanical stress prescribes cytoskeleton behavior in Arabidopsis cotyledon pavement cells. eLife 3: e01967

Sanati Nezhad A, Geitmann A (2015) Tip growth in walled cells: Cellular expansion and invasion mechanisms. *In* C Cuerrier and A Pelling, eds, Cells, Forces and the Microenvironment. Pan Stanford Publishing, Singapore, pp 335–356

Sapala A, Runions A, Routier-Kierzkowska AL, Das Gupta M, Hong L, Hofhuis H, Verger S, Mosca G, Li CB, Hay A, et al (2018) Why plants make puzzle cells, and how their shape emerges. eLife 7: e32794

Scarcelli G, Yun SH (2007) Confocal Brillouin microscopy for three-dimensional mechanical imaging. Nat Photonics 2: 39–43

Scarcelli G, Yun SH (2011) Multistage VIPA etalons for high-extinction parallel Brillouin spectroscopy. Opt Express 19: 10913–10922

Scarcelli G, Kim P, Yun SH (2011) In vivo measurement of age-related stiffening in the crystalline lens by Brillouin optical microscopy. Biophys J 101: 1539–1545

Scarcelli G, Polacheck WJ, Nia HT, Patel K, Grodzinsky AJ, Kamm RD, Yun SH (2015) Noncontact three-dimensional mapping of intracellular hydromechanical properties by Brillouin microscopy. Nat Methods 12: 1132–1134

Sotiriou P, Giannoutsou E, Panteris E, Galatis B, Apostolakos P (2018) Local differentiation of cell wall matrix polysaccharides in sinuous pavement cells: Its possible involvement in the flexibility of cell shape. Plant Biol (Stuttg) 20: 223–237

Suslov D, Verbelen JP (2006) Cellulose orientation determines mechanical anisotropy in onion epidermis cell walls. J Exp Bot 57: 2183–2192

Swaminathan V, Kalappurakkal JM, Mehta SB, Nordenfelt P, Moore TI, Koga N, Baker DA, Oldenbourg R, Tani T, Mayor S, et al (2017) Actin retrograde flow actively aligns and orients ligand-engaged integrins in focal adhesions. Proc Natl Acad Sci USA 114: 10648–10653

Szymanski DB (2014) The kinematics and mechanics of leaf expansion: New pieces to the Arabidopsis puzzle. Curr Opin Plant Biol 22: 141–148

Szymanski DB, Cosgrove DJ (2009) Dynamic coordination of cytoskeletal and cell wall systems during plant cell morphogenesis. Curr Biol 19: R800–R811

Szymanski DB, Staiger CJ (2018) The actin cytoskeleton: Functional arrays for cytoplasmic organization and cell shape control. Plant Physiol 176: 106–118

Thomas J, Idris NA, Collings DA (2017) Pontamine Fast Scarlet 4B bifluorescence and measurements of cellulose microfibril angles. J Microsc **268:** 13–27

Thomas LH, Forsyth VT, Sturcová A, Kennedy CJ, May RP, Altaner CM, Apperley DC, Wess TJ, Jarvis MC (2013) Structure of cellulose microfibrils in primary cell walls from collenchyma. Plant Physiol **161:** 465–476

Võfély RV, Gallagher J, Pisano GD, Bartlett M, Braybrook SA (2019) Of puzzles and pavements: A quantitative exploration of leaf epidermal cell shape. New Phytol **221:** 540–552

Winter D, Vinegar B, Nahal H, Ammar R, Wilson GV, Provart NJ (2007) An "Electronic Fluorescent Pictograph" browser for exploring and analyzing large-scale biological data sets. PLoS One **2:** e718

Yanagisawa M, Alonso JM, Szymanski DB (2018) Microtubule-dependent confinement of a cell signaling and actin polymerization control module regulates polarized cell growth. Curr Biol **28:** 2459–2466

Yun SH, Chernyak D (2018) Brillouin microscopy: Assessing ocular tissue biomechanics. Curr Opin Ophthalmol **29:** 299–305

Zerzour R, Kroeger J, Geitmann A (2009) Polar growth in pollen tubes is associated with spatially confined dynamic changes in cell mechanical properties. Dev Biol **334:** 437–446

Zhang C, Halsey LE, Szymanski DB (2011) The development and geometry of shape change in *Arabidopsis thaliana* cotyledon pavement cells. BMC Plant Biol **11:** 27